Article

Use of the Asymmetrical Chelating N-Donor 2-Imino-Pyridine as a Redox [Fe4S4] Cubane Surrogate at a Di-Iron Site Related to [FeFe]-Hydrogenases

Andrea Mele [1], Federica Arrigoni [2,*], Luca De Gioia [2], Catherine Elleouet [1,*], François Y. Pétillon [1], Philippe Schollhammer [1,*] and Giuseppe Zampella [2,*]

[1] Laboratoire de Chimie, Electrochimie Moléculaire et Chimie Analytique, UMR 6521 CNRS-Université de Bretagne Occidentale, CS 93837, 6 Avenue Le Gorgeu, CEDEX 3, 29238 Brest, France; chemandmele@gmail.com (A.M.); francois.petillon@univ-brest.fr (F.Y.P.)

[2] Department of Biotechnology and Bioscience, University of Milano-Bicocca, Piazza della Scienza 2, 20126 Milan, Italy; luca.degioia@unimib.it

* Correspondence: federica.arrigoni@unimib.it (F.A.); catherine.elleouet@univ-brest.fr (C.E.); philippe.schollhammer@univ-brest.fr (P.S.); giuseppe.zampella@unimib.it (G.Z.)

Abstract: Two complexes, related to the active site of [FeFe]-hydrogenases, $[Fe_2(CO)_4(\kappa^2\text{-pma})(\mu\text{-bdt})]$ (**1**) and $[Fe_2(CO)_4(\kappa^2\text{-pma})(\mu\text{-pdt})]$ (**2**) (bdt = benzene-1,2-dithiolate, pdt = propane-1,2-dithiolate) featuring the diaza chelate ligand trans-N-(2-pyridylmethylene)aniline (pma) were prepared, in order to study the influence of such a redox ligand, potentially non-innocent, on their redox behaviours. Both complexes were synthesized by photolysis in moderate yields, and they were characterized by IR, ^{1}H and ^{13}C{^{1}H} NMR spectroscopies, elemental analyses and X-ray diffraction. Their electrochemical study by cyclic voltammetry, in the presence and in the absence of protons, revealed different behaviours depending on the aliphatic or aromatic nature of the dithiolate bridge. Density functional theory (DFT) calculations showed the role of the pma ligand as an electron reservoir, allowing the rationalization of the proton reduction process of complex **1**.

Keywords: iron; dinuclear; diaza chelate; imino-pyridine; cyclic voltammetry; potential inversion; non-innocent ligand; redox ligand; DFT calculations; hydrogenases

1. Introduction

In the active site of hydrogenases, called the H-cluster (Scheme 1a), the role of electron shuttle towards the di-iron [Fe2S2] centre with an azapropanedithiolate bridge would be played by a cubane-like cluster [Fe4S4], covalently linked by a cysteine to the di-iron sub-site [Fe2S2] [1–9]. The high activity of the H-cluster for the electrocatalytic H^+/H_2 conversion indeed relies on a fine electronic balance of charges. To our knowledge, only one di-iron complex with a cubane [Fe4S4] has been reported [10], which shows the difficulty of synthesizing a model of the H-cluster in its integrity. Achieving a simple and efficient model featuring a surrogate of the [Fe4S4] sub-site remains a challenge. In this context, various redox ligands were combined with bio-inspired di-iron systems, in the hope that they could act as redox electron-reservoirs with non-innocent properties [11–14] as [Fe4S4], allowing a catalytic activity. Among these ligands, are included in particular chelating nitrogen donor ligands, such as 2,2′-bipyridine (bipy), 1,10-phenanthroline (phen), 2,2′-bipyrimidine (bpym), 2-(phenylazo)pyridine (pap) (Scheme 1b) [15–22]. In parallel, diphosphines such as bma (bma = 2,3-bis(diphenylphosphino)maleic anhydride), dppen (1,2-bis(diphenylphosphino)ethene), bpcd (4,5-bis(diphenylphosphino)-4-cyclopenten-1,3-dione), were combined with di-iron systems, but it was shown that they act as innocent bystanders when they are associated with di-iron {Fe2(CO)4(μ-dithiolate)} core [23–25]. Differently from other complexes with the general formula [Fe2(CO)4(κ^2-chelate)(μ-dithiolate)],

which either undergo ETC process (diphosphine) or a two-electron reduction centred on the di-iron core (bis-carbene) [26,27], the complexes [Fe$_2$(CO)$_4$(κ^2-bipy)(μ-xdt)] (xdt = pdt (propane-1,2-dithiolate) or bdt (benzene-1,2-dithiolate)) [15,16] would reduce according to a two-electron process, with a potential inversion [28], involving the 2,2′-bipyridine ligand. The second electron would be centred on the bipy framework, unlike the first one, which would be located on the di-iron core. An electrocatalytic mechanism similar to that of the complex [Fe$_2$(CO)$_6$(μ-xdt)] was proposed.


(a)   **(b)**
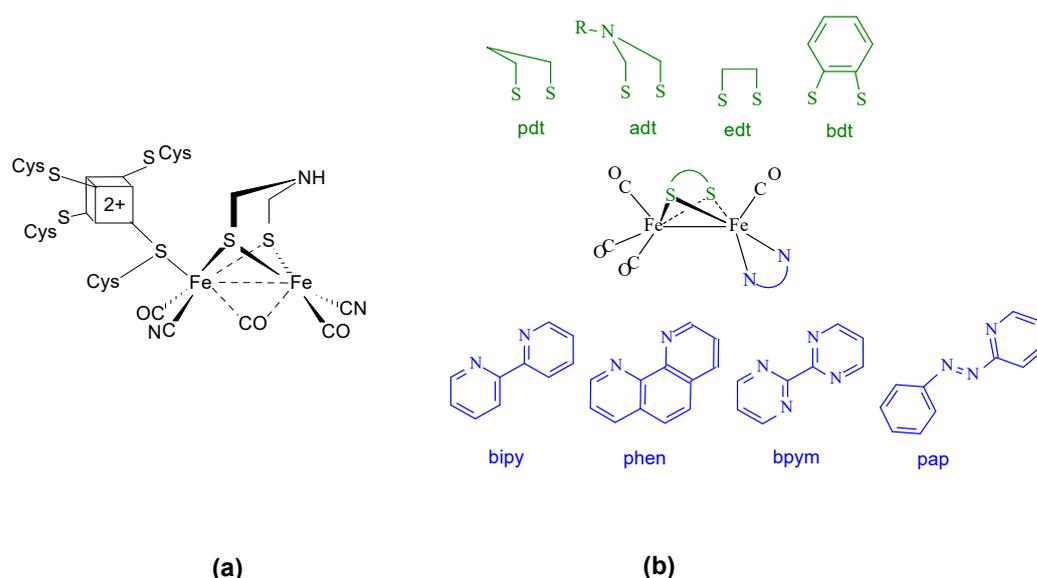
Scheme 1. H-cluster (**a**) and various di-iron complexes with chelating N-donor ligands (**b**).

Unlike its bipy analogue and the complex [Fe$_2$(CO)$_4$(κ^2-bpym)(μ-bdt)], the compound [Fe$_2$(CO)$_4$(κ^2-bpym)(μ-pdt)] affords two separate reductions with a ΔEp of 520 mV [15]. The first single-electron reduction is centred on the bpym ligand while the second reduction involves two electron transfers. One of these transfers arises at the metal atom, and the other one is centred on the ligand (bpym^{1-}/bpym^{2-}). Bpym is a better π-acceptor than bipy, which stabilizes the reduced metal centre due to the delocalization of the electronic density into the lower vacant π^* orbital. Unfortunately, this modification does not benefit the efficiency of the electrocatalytic activity towards proton reduction, due to an ill-suited site of protonation. To date, the sole reported example of a di-iron species involving a non-metallic non-innocent redox ligand with an electrocatalytic activity towards proton reduction processes is the complex [Fe$_2$(CO)$_5$(κ^1-phosphole)(μ-bdt)] [13]. The control exerted by the 1,10-phenanthroline ligand on the electronic properties of the di-iron core has been highlighted through electrochemical studies and DFT calculations, in the case of the complexes [Fe$_2$(CO)$_4$(κ^2-phen)(μ-xdt)] (xdt = pdt, adt$^{i\mathrm{Pr}}$) and [Fe$_2$(CO)$_4$(κ^2-phen)(μ-edt)] (edt = ethane-1,2-dithiolate), for which a two-electron reduction with a potential inversion is observed, as it is for their analogue [Fe$_2$(CO)$_4$(κ^2-bipy)(μ-edt)] [17,18]. DFT calculations show that the first electron is picked up by the N-chelate into a π^* orbital. The second electron transfer into a σ^*(Fe–Fe) orbital gives rise to an open-shell triplet dianion. For complexes [Fe$_2$(CO)$_4$(κ^2-phen)(μ-pdt)] and [Fe$_2$(CO)$_4$(κ^2-phen)(μ-adt$^{i\mathrm{Pr}}$)], the 1,10-phenanthroline ligand is also implicated during the two-electron reduction and ensures electronic communication with the di-iron site [18]. In this case, the formation of two isomers with either a cleavage of a Fe-S bond or the retention of the [Fe2S2] core is proposed. This suggests that different mechanisms for proton reduction may be induced in such di-iron systems using redox ligands. The non-innocent properties of 2-(phenylazo)pyridine (structurally similar to the 2,2′-bipyridine) have also been reported. They are due to highly delocalized metal–ligand hybrid molecular orbitals [22]. DFT calculations have shown that the HOMO (Highest Occupied Molecular Orbital) of [Fe$_2$(CO)$_4$(κ^2-pap)(μ-bdt)], and that of

its pdt analogue, are developed on the iron atoms carrying the redox ligand. The LUMO (Lowest Unoccupied Molecular Orbital) is a mixed metal–ligand orbital localized on the chelating ligand. The existence of a facile communication between the di-iron core and the diazo ligand was thus suggested. The protonation at the di-iron site should be favoured, while an overly negative reduction potential is avoided, thus affording the possibility to have a catalyst operating with low overpotential.

Herein is reported the study of di-iron complexes featuring a trans-N-(2-pyridylmethylene)aniline (pma) chelate, whose behaviour as an electron host has been highlighted [29–32]. The electrons may be delocalized on the entire pma ligand, modifying its geometry (via bond lengthening or shortening) (Scheme 2). The use of such pyridinyl-imine ligands affords interesting perspectives for controlling redox processes through both steric and electronic influences [29–32].
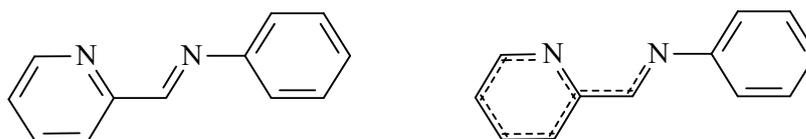

Scheme 2. Representation of the pma ligand and the possibility of π-electron delocalization.

DFT calculations have been carried out with the aim to clarify the non-innocent role of the pma ligand and establish whether and how modifications of the dithiolate bridge may impact the nature of the reduced species. Moreover, the proton reduction process, in the case of the complex $[Fe_2(CO)_4(\kappa^2\text{-pma})(\mu\text{-bdt})]$ (Complex **1**), was investigated.

2. Results and Discussion

2.1. Synthesis and Characterization

The complexes $[Fe_2(CO)_4(\kappa^2\text{-pma})(\mu\text{-bdt})]$ (**1**) and $[Fe_2(CO)_4(\kappa^2\text{-pma})(\mu\text{-pdt})]$ (**2**) (Scheme 3) were prepared by the UV photolysis of their hexacarbonyl precursors, $[Fe_2(CO)_6(\mu\text{-bdt})]$ and $[Fe_2(CO)_6(\mu\text{-pdt})]$, in the presence of trans-N-(2-pyridylmethylene)aniline (pma) (Appendix A). **1** and **2** were characterized by IR, NMR (^{1}H, ^{13}C) spectroscopies, elemental analysis and X-ray diffraction. The IR spectra of **1** and **2** display, in the carbonyl region, the typical pattern of unsymmetrically disubstituted species $[Fe_2(CO)_4(\kappa^2\text{-chelate})(\mu\text{-pdt})]$, consisting of three strong bands (Figure S1). The expected shift of the ν(CO) bands towards lower wavenumbers, compared to their hexacarbonyl parent complexes, is observed (Table S3). The average value of the ν(CO) bands is 1955 cm^{-1} for **2**, which corresponds to a red shift of 12 cm^{-1} compared to **1**, due to the replacement of the bdt bridge by a pdt one. Their comparison with those of compounds with 2,2′-bipyridine or 1,10-phenanthroline shows that these diaza ligands are better σ-donors than trans-N-(2-pyridylmethylene)aniline. **1** and **2** were also characterized by ^{1}H and ^{13}C{^{1}H} NMR in CD$_2$Cl$_2$. Their ^{1}H NMR spectra (Figures S2a and S3a) display the expected resonances for a (pyridylmethylene)aniline framework [29–31] linked to a metal centre, as well as the signals of the alkyl or aromatic chain of the dithiolate bridge. The coordination of the unsymmetrical chelating ligand pma causes the absence of chemical equivalency of the protons in the dithiolate bridge, which is also evidenced in the ^{1}H NMR spectrum of **2**. This dissymmetry is also revealed in the ^{13}C-{^{1}H} NMR spectrum of **2** in the {S(CH$_2$)$_3$S} region (Figure S3b). **1** and **2** display the same typical pattern in the carbonyl region with a resonance at *ca* 216 ppm, which is assigned to the terminal carbonyl of the {Fe(CO)N$_2$} fragment, and another singlet at *ca* 212 ppm for the three CO groups of the {Fe(CO)$_3$} moiety (Figures S2b and S3b). The signals of pma [29–31] and bdt groups are detected between 160 and 120 ppm.
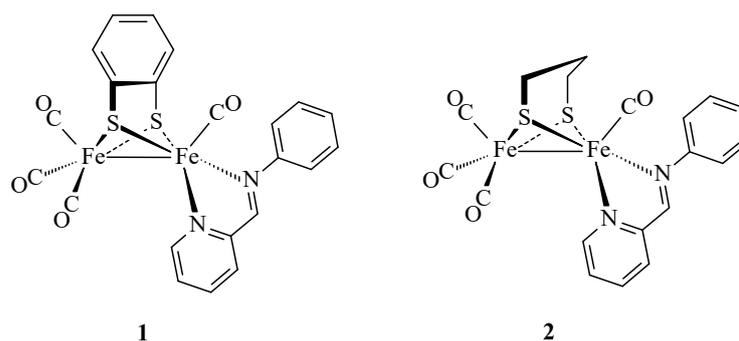
Scheme 3. Complexes **1** and **2**.

The UV–visible spectrum of **1** in CH_2Cl_2 was also recorded (Figure S4a). It mainly shows two bands of absorption at *ca* 300 nm and 648 nm. This latter band, which is responsible for the dark green colour of **1**, is observed neither in the spectrum of $[Fe_2(CO)_6(\mu\text{-bdt})]$ nor in that of the free ligand. The time-dependent DFT (TD-DFT) spectrum of **1** was calculated (M06-2X functional, see Section 3) (Figure S4b) [33]. It predicts the existence of an absorption band at 620 nm, which agrees with the observed transition (648 nm) for **1**. This absorption is attributed to a metal-to-ligand charge transfer mainly from the HOMO to the LUMO, which are metal- and ligand-based, respectively (Figure 1). Such an interaction is likely due to the strong π-acceptor ability of the ligand, which can compensate for its σ-donor character and that could explain an efficient delocalization of electrons between the di-iron core and pma. A key feature to establish this kind of communication is the direct connection between the di-iron core and the ligand through the two nitrogen atoms, which are included into a hetero-cycle where the electron density is highly delocalized. That is not observed with redox diphosphines, in which the sp^3 hybridized phosphorus atoms do not favour electron delocalization between the di-iron core and the rest of the diphosphine ligand. The observation of such a transition for **1** suggests an electron delocalization between the di-iron core and the pma ligand, which is crucial for having non-innocent behaviours.
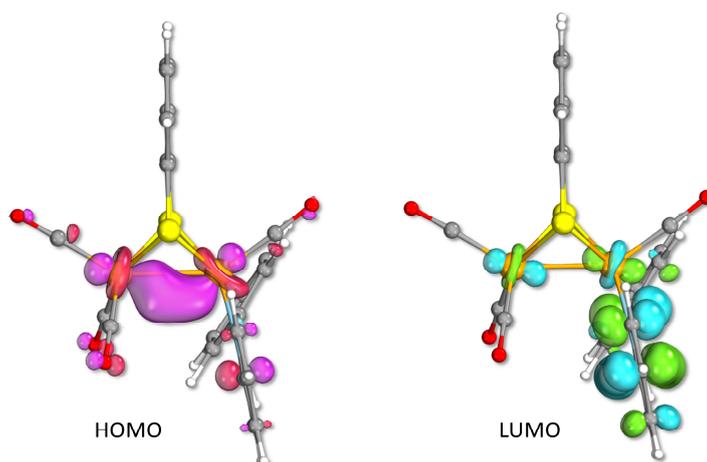

Figure 1. HOMO (**left**) and LUMO (**right**) of **1** (isosurface cutoff 0.05 a.u.).

Complexes **1** and **2** were crystallized from the slow evaporation of solutions of hexane/dichloromethane (1:1) at −30 °C, and their structures in solid states were determined by X-ray diffraction analyses (Figure 2, Tables 1, S1, S2 and S4). The two iron atoms in **1** and **2** have a distorted square pyramidal local geometry, with the pma ligand in a dibasal position at the Fe(1). The two compounds display a common eclipsed geometry, when considering the projection of the basal and apical bonds around each iron atom along the iron–iron axis. The replacement of the dithiolate bridge leads to some slight differences in the bond lengths observed in **1** and **2**, with those of the propanedithiolate complex being

slightly longer (Table 1). For example, the iron–iron distance in **2** is longer than that in **1** by 0.0305 Å. They are in the range of distances expected for single Fe(I)-Fe(I) bonds in such complexes. The Fe(1)-N distances are very close, despite their different chemical natures (i.e., pyridine vs. imine). The distance between the nitrogen atom of the pyridine and the Fe(1) is longer in **2** by 0.032 Å. The lengthening of some bonds reflects different electron donation behaviours of the aliphatic and aromatic dithiolate bridges and their own geometrical constraints. The N(1)-Fe(1)-N(2) bite angles are very close in the two complexes (80.47° in **2** and 81.4° in **1**). They are in the same range than those observed for other diaza ligands [15–22,34]. The C-N distance of the imine function is typical of that expected for a double C=N bond without important π-electron delocalization over the pma ligand, which is nevertheless revealed by the distance C(11)-C(12) [C_{pyr}-C_{imine}] of *ca* 1.42–1.44 Å. Other bond angles for the pma ligand in **1** and **2** can be found in Table S4. The Fe(1)-C(1)-(O1) angle deviates more from the linearity in **2** (172.9 °) than in **1** (176.8°), which is related to the nature of the organic linker of the dithiolate bridge. Finally, the overall geometries of **1** and **2** are very similar to those reported for the analogous bdt- and pdt-compounds with a (phenylazo)pyridine ligand [22].
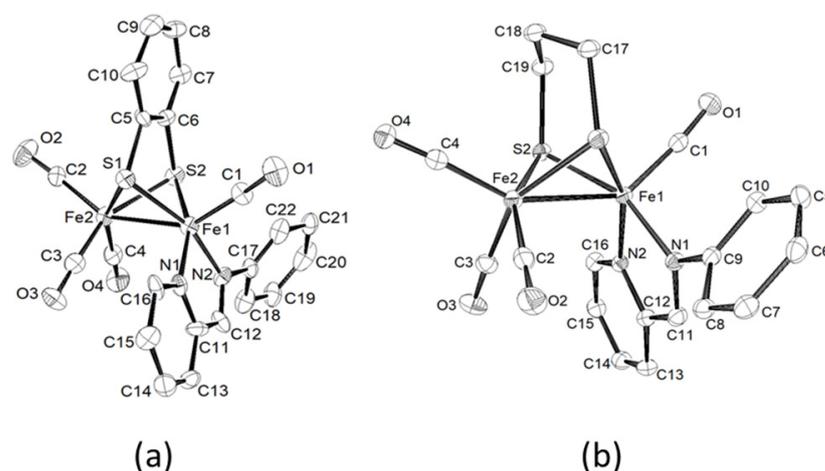
Figure 2. ORTEP view (ellipsoids at 30% of probability level) of **1** (**a**) and **2** (**b**).

Table 1. Selected bond lengths (Å) and angles (°) of **1** and **2**.

	1	2
Fe(1)-Fe(2)	2.505 (2)	2.5355 (5)
Fe(1)-S(1)	2.241 (4)	2.2183 (8)
Fe(2)-S(1)	2.270 (4)	2.2669 (8)
Fe(1)-S(2)	2.254 (3)	2.2179 (7)
Fe(1)-S(2)	2.281 (4)	2.2700 (8)
Fe(1)-N (*Ph*))	1.962 (11)	1.962 (2)
Fe(1)-N (*pyr*)	1.942 (11)	1.974 (2)
C(11)-C(12)	1.44 (2)	1.426 (4)
C(5)-C(6)	1.381 (4)	
C-N (*C=N imine*)	1.277 (18)	1.304 (3)
N-C (*ispo-Ph*)	1.436 (16)	1.432 (3)
C-N (*pyr*)	1.365 (18)	1.363 (3)
C16-N (*pyr*)	1.388 (18)	1.356 (3)
C(15)-C(16)	1.378 (4)	1.393 (19)
C(1)-O(1)	1.139 (16)	1.159 (3)
C(1)-Fe(1)	1.785 (14)	1.757 (3)
C-O (*apical-Fe(2)*)	1.145 (17)	1.144 (3)
C-Fe(2) (*apical*)	1.813 (15)	1.809 (3)
C(3)-O(3) (*basal-Fe(2)*)	1.223 (18)	1.154 (3)
Fe(2)-C(3)	1.717 (16)	1.779 (3)

Table 1. *Cont.*

	1	**2**
C-O (*basal-Fe(2)*)	1.167 (18)	1.149 (3)
Fe(2)C (*basal*)	1.748 (16)	1.778 (3)
Fe(1)-S(1)-Fe(2)	67.46 (11)	64.84 (2)
Fe(1)-S(2)-Fe(2)	67.07 (11)	68.79 (2)
Fe(1)-C(1)-O(1)	176.8 (14)	172.9 (3)
Fe(2)-C-O (*apical*)	177.0 (14)	176.5 (2)
Fe(2)-C(3)-O(3)	177.4 (15)	176.9 (3)
Fe(2)-C-O (*basal*)	178.6 (15)	178.3 (3)
N(1)-Fe(1)-N(2)	81.4 (5)	80.47 (9)

2.2. Electrochemical Behaviour of Complexes **1** *and* **2** *in the Absence and in the Presence of Acid*

The electrochemical behaviours of **1** and **2** were studied by cyclic voltammetry, using a glassy carbon electrode in CH_2Cl_2-$[NBu_4][PF_6]$ 0.2 M (Figure 3). The replacement of the bdt bridge by pdt leads to a shift of the potential towards more negative values, consistent with the red shift observed in the IR spectrum (Table S3), indicating the electronic effect of the bridge (Table 2). Moreover, the oxidation of **1** is irreversible while that of **2** is partially reversible. The comparison of the oxidation and reduction current intensities suggests that the number of electrons involved are the same in reduction and oxidation (one electron for **2** and two electrons for **1** at 0.2 Vs^{-1}). The reduction of **2** is followed by an irreversible reduction at -2.38 V, which implies the transfer of two supplementary electrons. This further electron transfer is absent in the case of **1**.
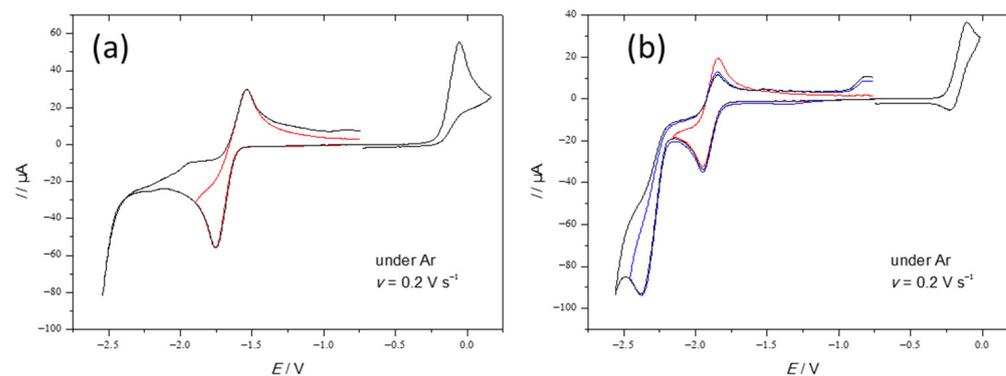

Figure 3. Cyclic voltammograms of (**a**) **1** (1.45 mM); (**b**) **2** (1.44 mM) in CH_2Cl_2-$[NBu_4][PF_6]$ (0.2 M) under Ar at 0.2 Vs^{-1}.

Table 2. Potentials of reduction and oxidation at 0.2 Vs^{-1}.

Compound	$Ep^{c,red}$/V	$(``E_{1/2}{}^{red}")$/V	$Ep^{a,ox}$/V
$[Fe_2(CO)_4(\kappa^2$-pma$)(\mu$-bdt$)]$ (**1**)	-1.76	(-1.66)	-0.04
$[Fe_2(CO)_4(\kappa^2$-pma$)(\mu$-pdt$)]$ (**2**)	-1.95	(-1.89)	-0.11

The scan rate dependence of the current function of **1** (Figure 4, Figures S5 and S6 for **2**), compared with that of the single-electron oxidation of $[Fe_2(CO)_4(\kappa^2$-I_{Me}-CH_2-$I_{Me})(\mu$-pdt$)]$ [26], shows that **1** transitions from a two-electron (slow scan rates) to a one-electron process (fast scan rates), which is consistent with an ECE-type mechanism. Indeed, the reduction of **1** occurs according to a process similar to that of $[Fe_2(CO)_6(\mu$-bdt$)]$. It is worth noting that, in the case of $[Fe_2(CO)_4(\kappa^2$-phen$)(\mu$-pdt$)]$, the two-electron reduction at 0.2 Vs^{-1} splits into two one-electron reduction steps at 40 Vs^{-1} [18]. No splitting was observed for **1**.
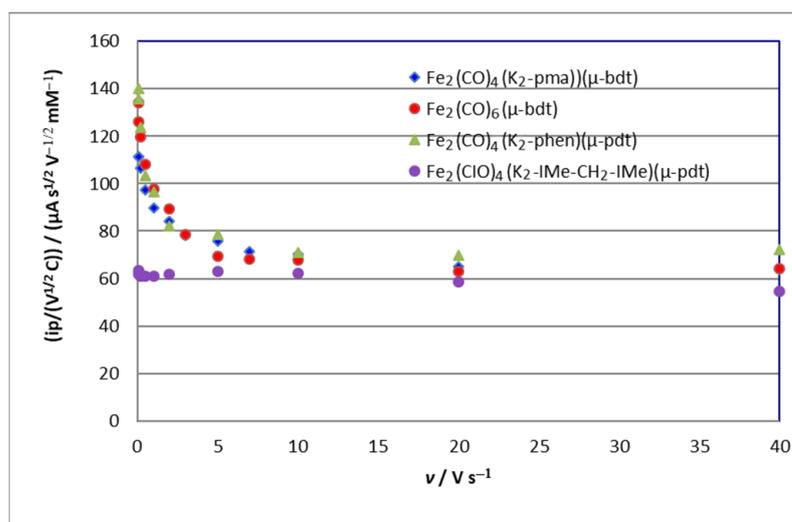
Figure 4. Scan rate dependence of the current function of various complexes [Fe$_2$(CO)$_4$(κ^2-chelate)(μ-xdt)] and [Fe$_2$(CO)$_6$(μ-bdt)], in CH$_2$Cl$_2$-[NBu$_4$][PF$_6$] (0.2 M) under Ar.

Acetic acid is not strong enough to protonate **1** and **2** (Figure S7). There is no catalysis at the reduction potential of the neutral complexes, although there is an increase, roughly double, of the current at this potential in the case of **2** (Figure 5). Nevertheless, the new peak near −2.1 V for **1**, whose intensity increases with additions of acid, suggests that the reduced form is protonated, and that the catalysis arises at the potential of reduction of the protonated species that is generated.
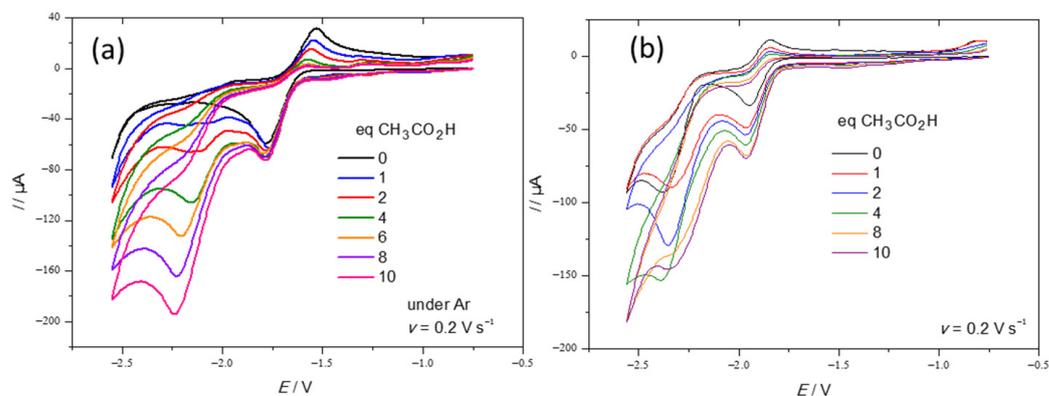
Figure 5. Reduction of **1** (1.26 mM) (**a**) and **2** (1.44 mM) (**b**) in the presence of CH$_3$CO$_2$H in CH$_2$Cl$_2$-[NBu$_4$][PF$_6$] (0.2 M) under Ar at 0.2 Vs^{-1}.

Unlike CH$_3$CO$_2$H, CF$_3$CO$_2$H protonates both **1** and **2**. This results in the decrease of the oxidation peak of the neutral complexes (Figure S8b) and in the appearance of a peak at −1.7 V for **2** after the addition of one equivalent of CF$_3$CO$_2$H (Figure S8a). A catalytic current is observed at this potential upon further additions. New peaks appear at −1.0 V and −1.3 V when four equivalents of acid are added, suggesting the supplementary protonation of the species in solution.

In order to rationalize the difference between the behaviour of **1** and **2** and to compare them with that of the analogue [Fe$_2$(CO)$_4$(κ^2-phen)(μ-pdt)], their reductive processes were theoretically investigated. The reduction mechanism of **1** in the presence of protons was also studied using DFT calculations.

2.3. Density Functional Theory Investigation of Geometries and Electronic Structures of the Anionic Species Arising from the Reduction of Complexes **1** and **2**

For each anionic species of **1** and **2**, a systematic thermodynamic speciation study of their various possible geometries was carried out. This allowed for the computation of the redox potentials for the most stable structures.

The isomers speciation of the elusive **1**$^-$ (Figure 6a) was performed while considering the two possible regiochemical alternatives for the Fe-S bond breaking (Figure 6b).
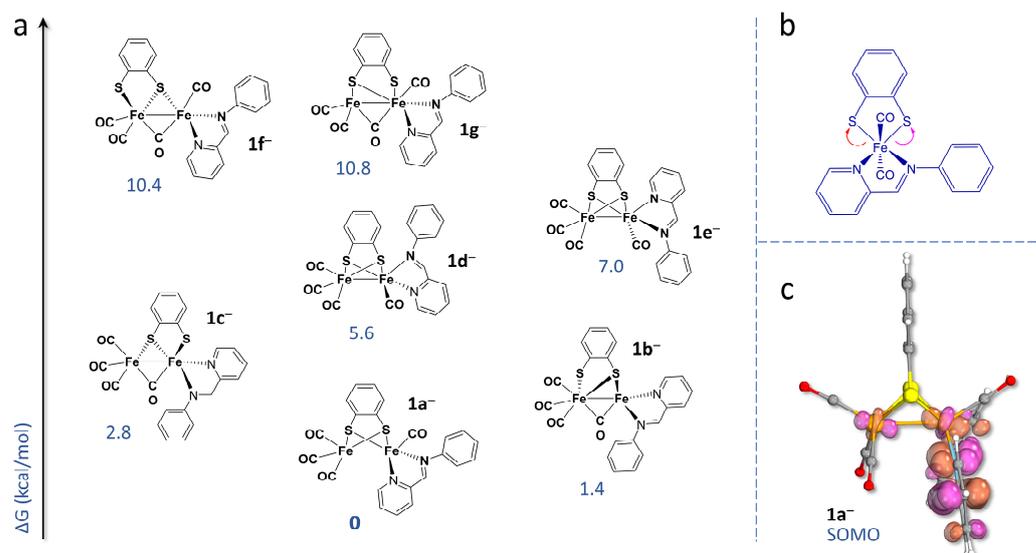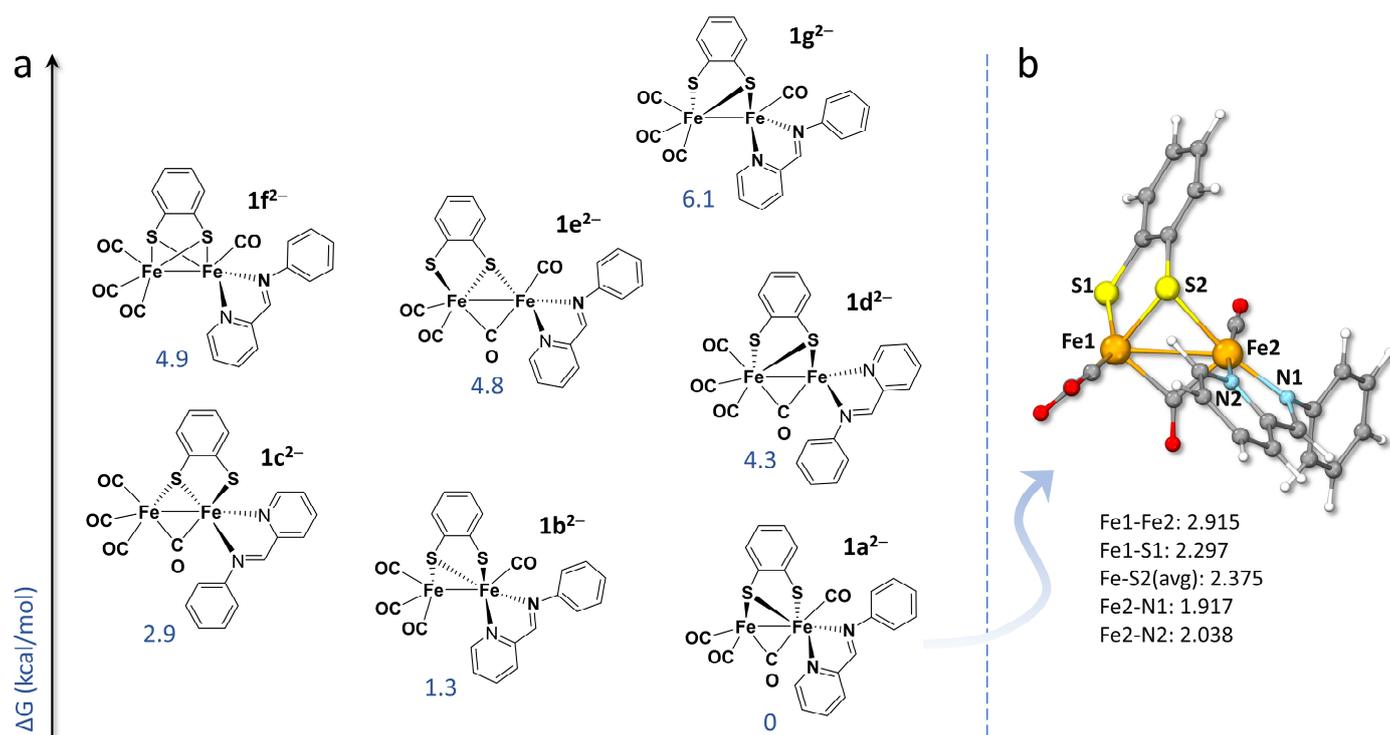

Figure 6. (**a**) DFT thermodynamic speciation of **1**$^-$ isomers. (The anionic nature of all structures reported is implicit, thus omitted for clarity). (**b**) The two different regiochemical alternatives for the Fe-S bond breaking; (**c**) SOMO of **1a**$^-$ (isosurface cutoff 0.05 a.u.).

The geometry of the most stable isomer (**1a**$^-$) corresponds to that of the neutral precursor, the only difference being an overall elongation of all bond lengths. The isomers **1b**$^-$ and **1c**$^-$ (Figure 6a), arising from the rotation around the FeFe axis of the {Fe(pma)CO} moiety, in which the apical CO adopts a bridging position and the pma ligand lies in a dibasal disposition, turned out to be only slightly disfavoured compared to the ground state. The description of the higher-energy isomers, as well as details on the geometrical and electronic properties of **1a**$^-$, are given in Figure S9. In the isomer **1a**$^-$, the Fe-Fe bond is stretched (ca 0.387 Å) upon reduction of **1**, due to the antibonding σ* character of the singly occupied molecular orbital (SOMO) of the anionic product. This latter is described as the combination of a σ*(Fe-Fe) orbital mixed with π* ligand-based orbitals, leading to an overall delocalized metal–ligand molecular orbital (Figure 6c). The geometry of the pma ligand is consequently modified and the double bonds are elongated while the σ-bonds are shortened. These changes suggest that the electron is delocalized on the entire pma ligand (Figure S9). The Fe–S distances do not change significantly, and the Fe–CO lengths suggest that the additional electron does not significantly involve this portion of the complex.

The theoretical redox potential for the first electron transfer is −1.68 V, close to the experimental value of −1.66 V vs. (Fc$^+$/Fc). The single electron density is delocalized over the pma ligand and partially over the metal core. This is in agreement with the analysis of **1a**$^-$ spin density, showing that the unpaired electron is shared between the di-iron core and pma (Figure S9). Interestingly, the highest value of spin density is found on nitrogen and iron atoms. In detail, the chelated Fe atom bears more spin density than the other, probably due to the coordination of the diaza chelate (Figure S9). It is also noticeable that the iminic nitrogen is more populated than the pyridinic one. Finally, this electronic delocalization suggests a non-innocent redox character of the pma ligand (as expected from the interpretation of the UV–visible spectrum).

Unlike **1a⁻**, the ground state for the dianion **1a²⁻** does correspond to the structure of the neutral species (Figures 7 and S10). The most stable isomers (**1a²⁻**, **1b²⁻**, **1c²⁻**) features a broken Fe-S bond that involves the {Fe(CO)₃} unit. Isomers without a broken Fe-S bond (**1f²⁻**), or in which its breaking involves the {Fe(CO)pma} unit (**1d²⁻**, **1e²⁻**, and **1g²⁻**), are higher in energy by 4–6 kcal/mol, with respect to **1a²⁻**. The rearrangement observed in **1a²⁻** is consistent with the existence of a chemical event during the two-electron process, as suggested by the electrochemical study at slow scan rates. The computed redox potential for the second electron transfer is −1.20 V vs. (Fc⁺/Fc) which indicates that this reduction has a potential lower than the first one, as reported for its precursor [Fe₂(CO)₆(μ-bdt)] [35–37] and other di-iron complexes [28,38–40].

Figure 7. (**a**) DFT thermodynamic speciation of **1²⁻** isomers. (The anionic nature of all structure reported is implicit, thus omitted for clarity). (**b**) Optimized structure of **1a²⁻**, with relevant geometrical parameters (in Å).

The total distribution of the charge in **1a²⁻** is −1.7 on the di-iron core and −0.3 on the pma ligand. The difference between these values and those determined for the mono-anion **1a⁻** suggests that the charge at the di-iron core is enriched, and that of the pma depleted, which supports the non-innocent behaviour of the pma ligand.

The more stable mono-reduced isomers **2a⁻** and **2b⁻** (Figures 8 and S11) have similar structures, differing only through an Fe-Fe bond stretching in the isomeric ground state (**2a⁻**), which suggests an (FeFe) antibonding character of the SOMO. This latter, like that of **1⁻**, is a delocalized hybrid metal–ligand molecular orbital, mixing σ*(Fe-Fe) and π* pma ligand orbital contributions. As expected, slight variations of pma distances are also indicative of a delocalization of the electron over the ligand. The spin density analysis (Figure S11c) is consistent with the SOMO orbital character, with a preferential distribution on the pma ligand over the di-iron core. A slight increase in the percentage of electronic density on the di-iron core, compared to **1⁻**, may be related to the different electronic properties of the bdt and pdt bridges. The redox potential calculated for the first electron transfer is −1.86 V vs. (Fc⁺/Fc), in agreement with the experimental one of −1.89 V vs. (Fc⁺/Fc).
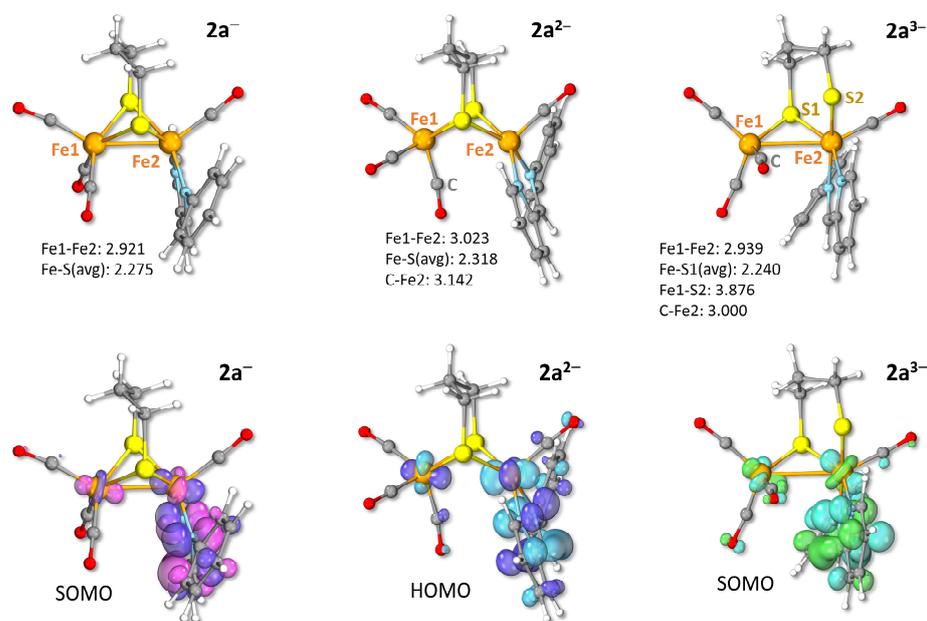
Figure 8. Optimized structure of the most stable reduced isomers of **2**. Selected distances (in Å) and frontier molecular orbitals (isosurface cutoff 0.05 a.u.) are also shown.

In the most stable bi-reduced form, **2a^{2-}**, one CO adopts a semi-bridging position, and the FeFe interaction is weakened (Figures 8 and S12). The Fe-S bond cleavage predicted for **1^{2-}** is not favoured in the case of the pdt dianion. Upon the addition of a second electron, a stretch of the Fe-S bond (ca 0.102 Å) is observed at the less substituted metal centre. The geometry of the species is only slightly modified, consistent with the electrochemical observations that show the absence of a chemical process between the first and the second reduction. There is a slight shortening of the Fe-N bonds (ca 0.05 Å), which might be related to a strengthened coordination of the pma ligand. The theoretical value of the second electron transfer is −2.33 V, close to the experimental value (−2.36 V). The main difference between **1^{2-}** and **2^{2-}** is the absence of any significant structural rearrangement in the case of the latter. The HOMO of **2^{2-}** (Figure 8) has a slightly prevalent pma ligand character, which shows, however, that the electronic density is roughly distributed over the entire structure. Accordingly, the charge in **2^{2-}** is equally shared between the di-iron core (−1.02) and the pma ligand (−0.98). This shows that the second electron is mainly transferred onto the di-iron core, allowing a global re-balancing of the electronic charge.

The electrochemical study of **2** suggests that the second reduction occurs, according to an ECE mechanism. For this reason, the relative stability of different isomers of **2^{3-}** was investigated. The most stable isomer (**2a^{3-}**) features a Fe-S cleavage, which could be the chemical rearrangement associated with the reduction at −2.36 V. The computed redox potential for the transfer of a third electron is −1.94 V vs (Fc$^+$/Fc), which is in accordance with the proposed electrochemical process. The SOMO of **2^{3-}** is a delocalized hybrid metal–ligand molecular orbital with σ*(Fe-Fe) and π* pma ligand-based orbital contributions, with this latter being predominant (Figure 8). The spin density analysis (Figure S13) shows, as expected, that 73% of the electronic density dwells on the pma ligand and 27% on the di-iron core.

2.4. Density Functional Theory Investigation of the Mechanism of Proton Reduction for Complex **1**

The rare combination of a redox ligand (pma) and an electron-withdrawing dithiolate bridge (bdt) in **1** prompted us to explore the process underlying the electrochemical reduction of this complex in the presence of acetic acid. The behaviour of its hexacarbonyl analogue [Fe$_2$(CO)$_6$(μ-bdt)] towards HER process (HER = Hydrogen Evolution Reaction) is well known [35–37,41], thus allowing straight comparisons and rationalization.

It is worth noting that the monoanion was demonstrated not to be protonated with acetic acid [42]. Three proton binding sites were highlighted; the proton can be attached to the di-iron core in a bridging position, to one iron atom in a terminal position or to a sulfur atom [43]. N-protonation occurs in the case of the complex $[Fe_2(CO)_6(\mu\text{-}S_2C_4N_2)]$ [44]. A thermodynamic speciation of the various protonated species was performed, in order to determine the most stable intermediates involved in the electrocatalytic cycle. The postulated mechanism (Figure 9) consists of an initial two-electron reduction of the complex, generating the dianionic active species. The following step is the protonation of this latter species, yielding a bridging hydride intermediate whose reduction allows the protonation of the dianion formed and finally triggers the formation and release of H_2.
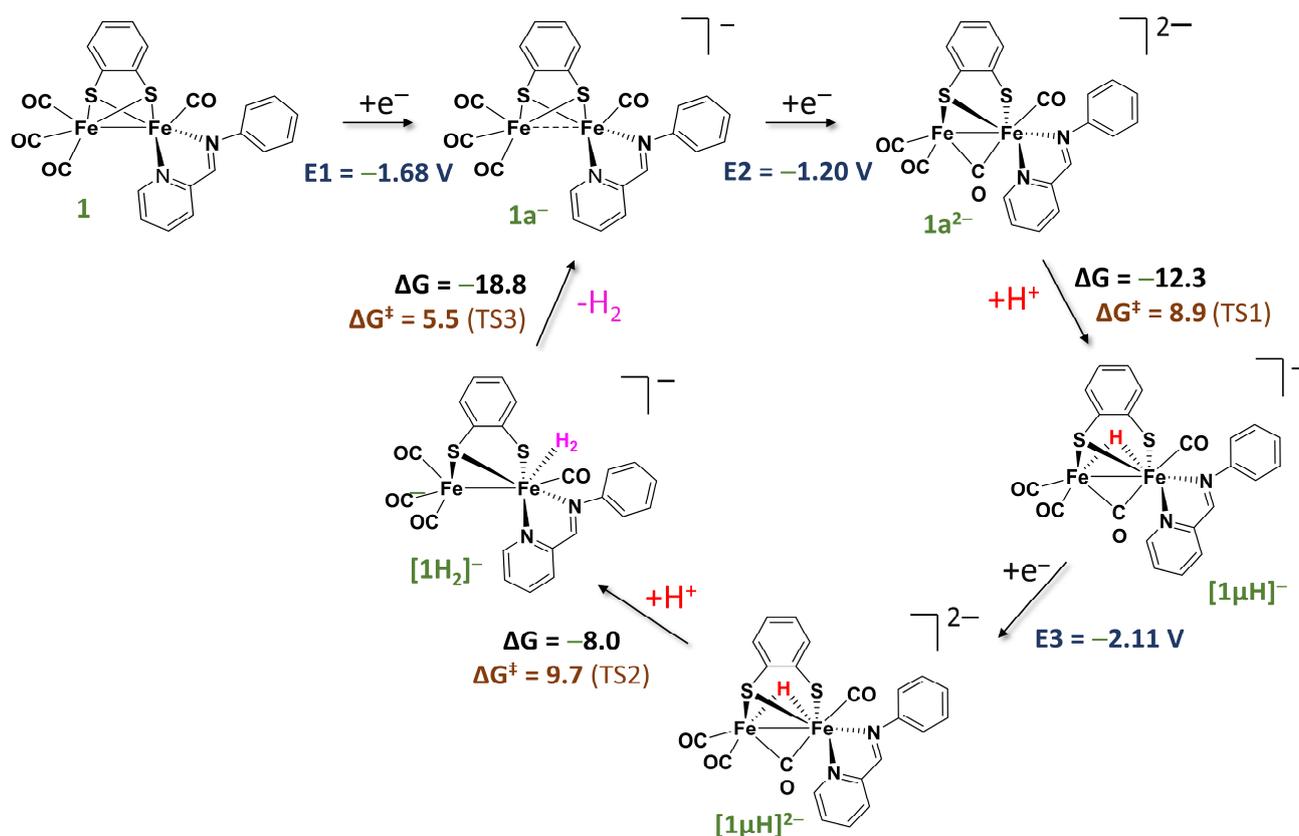
Figure 9. Calculated catalytic HER mechanism proposed for **1** in CH_2Cl_2 (free energy values are in kcal/mol).

The possible protonation sites of the isomer $\mathbf{1a^{2-}}$ were considered (Figure S14). N-protonation (pyridine and imine of the pma ligand), as well as S-protonation, are highly unfavourable. On the opposite hand, the bridging hydride form $\mathbf{[1\mu H]^-}$ is the most stable protonated isomer (Figure 10). The hydride ligand is asymmetrically bridged due to the difference of substitution of the two metal centres. The first protonation is exergonic ($\Delta G = -12.3$ kcal/mol), with an energy barrier of 8.9 kcal/mol. The related transition state (**TS1**, Figure 10) corresponds to a proton transfer from the acetic acid generating a terminal hydride at the chelated iron moiety, which then evolves into a bridging form. In the case of the hexacarbonyl dianion $[Fe_2(CO)_6(\mu\text{-}bdt)]^{2-}$, the value of the free energy (ΔG) of protonation and that of the activation barrier ($\Delta G^{\ddagger}$) are -7.0 kcal/mol and 17.2 kcal/mol, respectively. The comparison of these two parameters with those of $\mathbf{1^{2-}}$ suggests that the latter is more easily protonated, as expected.

Fe1-Fe2: 2.536
Fe1-H: 1.801
Fe2-H: 1.576

[1μH]⁻

Fe1-Fe2: 2.541
Fe1-H: 1.783
Fe2-H: 1.583

[1μH]²⁻

Fe1-Fe2: 2.884
Fe2-H1: 1.637
Fe2-H2: 1.621
H1-H2: 0.856

[1H₂]⁻

Fe1-Fe2: 2.658
Fe1-H: 1.685
Fe2-H: 2.447
O-H: 1.513

TS1

Fe1-H1: 1.584
Fe1-H2: 1.927
O-H2: 1.528
H1-H2: 0.925

TS2

Fe1-Fe2: 2.931
Fe2-H1: 1.836
Fe2-H2: 1.878
H1-H2: 0.816

TS3
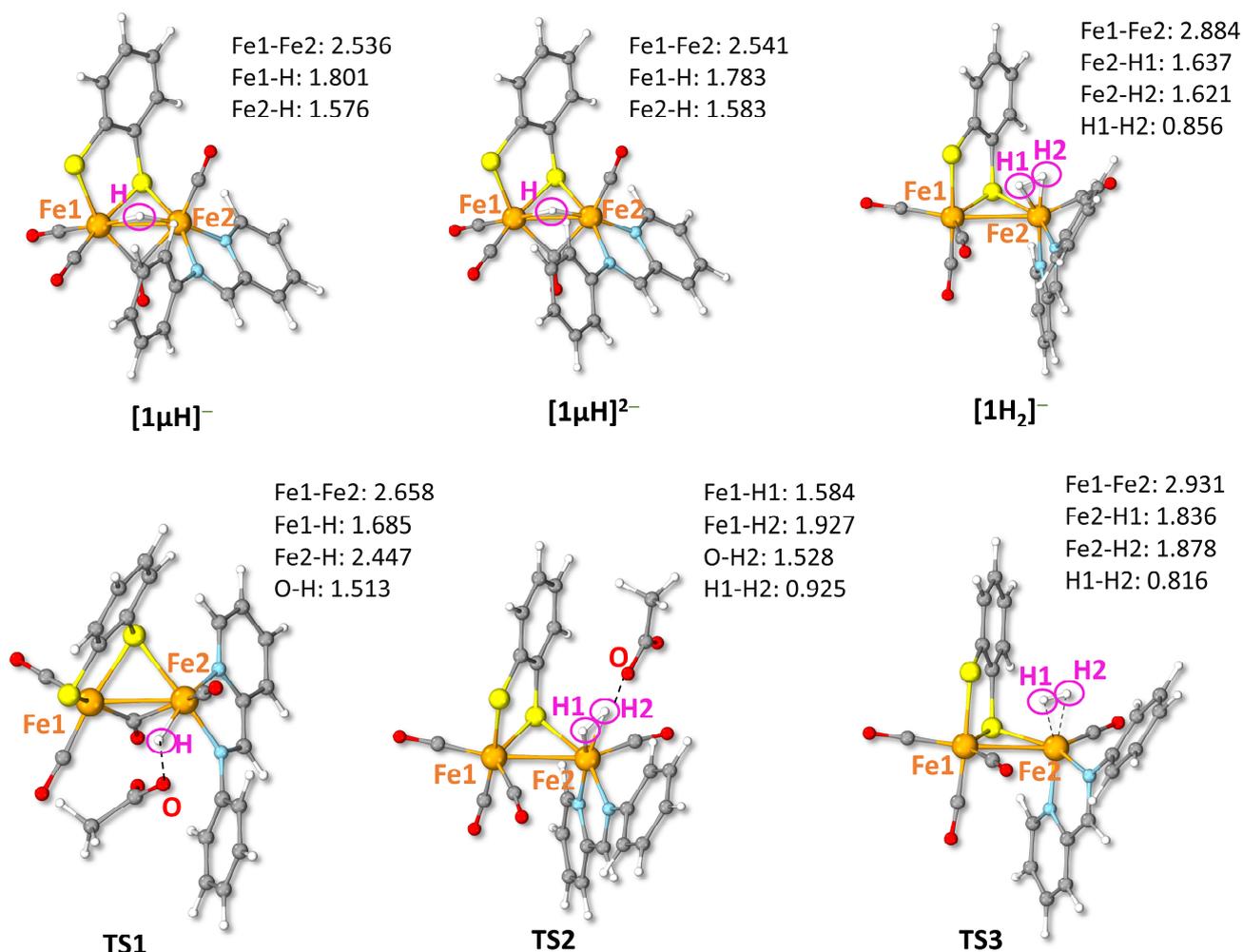
Figure 10. DFT-optimized structure of the protonated intermediates of 1 and transition states involved in the calculated HER mechanism (see also Figure 9). Selected distances in Å.

A further protonation of **[1μH]⁻** is not observed with CH_3CO_2H, suggesting that this species is not sufficiently basic to react with such a weak acid. The observation of a catalytic reduction of protons at −2.10 V indicates that a further addition of an electron is required to trigger the formation of H_2. The DFT reduction potential for the third electron transfer is −2.11 V, in agreement with the experimental one. The major structural change upon this reduction (**[1μH]²⁻**, Figure 10) is the planarization of the pma ligand. This rearrangement suggests that the third electron is mostly hosted on the diazo ligand. The spin density analysis shows that the electron density is mainly on the pma ligand (84%), with the remaining 16% being on the di-iron core (Figure S15).

As for **1²⁻**, the N-protonation and S-protonation of **[1μH]²⁻** do not lead to thermodynamically stable isomers (Figure S16). The most stable protonated form is the η^2-H_2 species **[1H₂]⁻**. A CO group, initially in the bridging position in **[1μH]²⁻**, moves to a basal position at the less substituted Fe atom upon this protonation step. As expected, the H-H bond is longer than in free H_2. An asymmetric distribution of the electron density is evidenced, with a prevailing contribution over the ligand atoms (Figure S15). The transition state of the second protonation step (**TS2**, Figure 10) and **[1H₂]⁻** display similar geometries. The free energy of this step is −8.0 kcal/mol, evidencing an exergonic process, and its activation barrier is + 9.7 kcal/mol (Figure 9). The geometry of the transition state, corresponding to the release of H_2 (**TS3**, Figure 10), presents elongated Fe-H distances (~0.2 Å), compared to those of the σ-H_2 species **[1H₂]⁻**, while the H-H bond is shorter (0.109 Å).

The H_2 detachment is exergonic ($\Delta G = -18.8$ kcal/mol) and fast ($\Delta G^{\ddagger} = 5.5$ kcal/mol), as shown in Figure 9.

3. Materials and Methods

All the experiments were carried out under an inert atmosphere, using Schlenk techniques for the syntheses. Solvents were deoxygenated and dried, according to standard procedures. The iron precursor [$Fe_2(CO)_6(\mu$-pdt)] [45,46] and [$Fe_2(CO)_6(\mu$-bdt)] [47] were prepared according to procedures set out previously in the literature. All other reagents were commercially available and used as purchased. NMR spectra (^{1}H and ^{13}C) were recorded with a Bruker (Billerica, MA, USA) DRX500 spectrometer of the "Service général des plateformes, Université de Bretagne Occidentale, Brest" and were referenced to SiMe$_4$ (^{1}H). The infrared spectra were recorded on a Perkin Elmer (Waltham, MA, USA) Spectrum 2 spectrometer. Chemical analyses were made by the "Service de Microanalyse I.C.S.N.", Gif sur Yvette, France. Electrochemical measurements were conducted using a PG-STAT 128 N Autolab or a μ-autolab (type III) electrochemical analyzer, driven by GPES 4.9 software. All the electrochemical studies were carried out in a conventional three-electrode cell under an inert atmosphere (argon). The preparation and the purification of the supporting electrolyte [Bu_4N][PF_6] were conducted as described previously [48]. The working electrode was a vitreous carbon disk of 0.3 cm in diameter, polished with alumina prior to use. A platinum wire was used as the counter electrode. The reference electrode was an Ag | Ag$^+$ electrode. All the potentials (text, tables, and figures) are quoted against the (Fc$^+$/Fc) couple. Ferrocene was added as an internal standard at the end of the experiments. Crystal data for complexes **1** and **2** were collected with an Oxford Diffraction X-Calibur-2 CCD diffractometer, equipped with a jet cooler device and graphite-monochromated Mo-K radiation ($\lambda = 0.71073$ Å). The structure was solved and refined by standard procedures [49]. The deposition numbers CCDC 22800462 and 22800460 contain the supplementary crystallographic data for **1** and **2**, respectively. These data can be obtained free of charge from the Cambridge Crystallographic Data Centre via www.ccdc.cam.ac.uk/data_request/cif (accessed on 15 June 2023).

DFT Modelling

Calculations were performed using the TURBOMOLE 7.4.1 suite of programs [50]. A triple-ζ TZVP basis (for all atoms) and the pure functional BP86 were used [51–53]. This particular basis-set/functional combination has been widely validated in the context of Fe/Ni thiolate bioinorganic and biomimetic systems, and also in relation to hydrogenases [54–57]. The Resolution of Identity (RI) technique allowed us to speed up the geometry optimizations [58].

Grimme's corrections with Becke–Johnson damping (D3BJ) were added to account for dispersive interactions [59,60]. COnductor-like Screening MOdel (COSMO) was used to implicitly treat the solvent, by setting a $\varepsilon_r = 8.93$ of CH_2Cl_2 [61,62]. The nature of each stationary point was verified by means of full vibrational analysis. Atomic charges and spin densities were calculated by performing a natural population analysis (NPA), as implemented in the natural bond orbital (NBO) procedure. The total partition function (Q) was evaluated as a product of q-rotational, q-translational and q-vibrational contributions and was used to derive free energies from SCF energy values, by setting temperature and pressure to 298.15 K and 1 bar, respectively (the scaling factor for the SCF wavenumbers was set to 0.9914, as the default value in TURBOMOLE for the adopted theoretical scheme). The UV spectrum of **1** was calculated with time-dependent DFT (TD-DFT), using the M06-2X functional [33]. The performance of other functionals was also tested, showing negligible variations with respect to M06-2X results. In-solvent free energies were used to calculate the absolute redox potentials of the complexes under investigation, according to the relation $E° = -\Delta G° /nF$ (n = number of electrons involved in the redox process; F = Faraday constant), which were then scaled by a reference value (-5.08 V for the Fc$^+$/Fc couple, calculated at the same level of theory).

4. Conclusions

The role of the imino-pyridine ligand (pma) as an electron reservoir in the dinuclear complexes **1** and **2** has been highlighted. The redox character of the pma ligand allows to understand why the electrochemical behaviour of the complex $[Fe_2(CO)_4(\kappa^2\text{-pma})(\mu\text{-pdt})]$ (**2**) is different than that of its hexacarbonyl analogue. While the latter undergoes a chemically reversible two-electron reduction at moderately negative potentials (ca. -1.2 V), for which the two electron transfers can be discriminated depending on the solvent and the scan rate, the former has a single-electron reversible reduction at -1.95 V, followed by a two-electron irreversible one at -2.38 V at slow scan rates.

The delocalization of the electronic charge on the pma ligand would prevent the triggering of the process involving two electrons and leading to the breakdown of the Fe-S bond. This process only occurs when a very negative potential is applied. It is worth noting that the redox behaviour of the pma complexes also depends strongly on the nature of the dithiolate bridge.

When the pdt bridge is replaced by an electron-withdrawing bridge like bdt, the presence of the pma redox ligand does not modify the redox behaviour of **1**, compared to its hexacarbonyl precursor, despite the ability of pma to retrieve a part of the electronic density upon reduction. The complex **1** is reduced at a more negative potential, due to the replacement of two CO groups by the diazo chelate, according to a two-electron mechanism (potential inversion). It is worth noting that, while the electronic density of the first transfer is mostly localized on the diaza chelate, after the second electron transfer it is located on the di-iron core.

It has been demonstrated that the phenanthroline ligand also has a non-innocent character in the complex $[Fe_2(CO)_4(\kappa^2\text{-phen})(\mu\text{-pdt})]$ that is different from that of the pma in **2**, allowing the concomitant presence of isomers with or without a broken Fe-S bond.

Finally, the pma ligand can interplay into the redox behaviour of complexes **1** and **2**, but the mechanism for the reductive proton process with **1** is very similar to that of its precursor $[Fe_2(CO)_6(\mu\text{-bdt})]$, with the need for a third electron transfer to allow the electrocatalytic reduction to occur. Extension to other pyridinyl-imines, by varying substituents at the aryl group or by replacing the phenyl, are now under examination, as well as useful and accessible oxazolyl pyridine/quinolone ligands.

Supplementary Materials: The following supporting information can be downloaded at: https://www.mdpi.com/article/10.3390/inorganics11120463/s1. Table S1: crystal data and structure refinement for complex **1**; Table S2: crystal data and structure refinement for complex **2**; Table S3: CO vibrational stretching frequencies for complexes **1**, **2** and analogous di-iron complexes in CH_2Cl_2; Table S4: selected angles (°) of the ligand pma in **1,2**; Figure S1: IR (CH_2Cl_2) spectra of **1** (a) and **2** (b) in carbonyl region; Figure S2: ^1H NMR (a) and $^{13}C\{^1H\}$ (b) NMR spectra of **1** in CD_2Cl_2 at 298 K; Figure S3: ^1H NMR (a) and $^{13}C\{^1H\}$ (b) NMR spectra of **2** in CD_2Cl_2 at 298 K; Figure S4: experimental UV–visible spectrum of **1** in CH_2Cl_2 (a); theoretical UV–visible spectrum of **1** (b); Figure S5: scan rate dependence of the reduction peak of **1** in CH_2Cl_2-[NBu$_4$][PF$_6$] (0.2 M) under Ar; Figure S6: scan rate dependence of the reduction peak of **2** in CH_2Cl_2-[NBu$_4$][PF$_6$] (0.2 M) under Ar; Figure S7: oxidation of **1** (1.26 mM) (a) and **2** (1.44 mM) (b) in the presence of CH_3CO_2H in CH_2Cl_2-[NBu$_4$][PF$_6$] (0.2 M) under Ar at 0.2 Vs^{-1}; Figure S8: CV, reduction (a) and oxidation (b), of **1** (1.39 mM) and **2** (1.46 mM) in the presence of CF_3CO_2H in CH_2Cl_2-[NBu$_4$][PF$_6$] (0.2 M) under Ar at 0.2 Vs^{-1}; Figure S9: (a) optimized structure of **1a**$^-$, with details on selected geometrical parameters and their comparison with **1**. (b) Spin density plot of **1a**$^-$ with related single contribution values to the total spin density for selected atoms. (c) Calculated IR νCO bands of **1a**$^-$; Figure S10: (a) HOMO of **1a**$^{2-}$ (isosurface cutoff 0.05 a.u.), showing a mixed metal–ligand character. (b) Calculated IR νCO bands of **1a**$^{2-}$; Figure S11: (a) thermodynamic speciation of **2**$^-$. (The anionic nature of all structure reported is implicit, thus omitted for clarity). (b) Theoretical IR spectrum in the νCO region (in CH_2Cl_2) of **2a**$^-$. (c) Spin density plot in **2a**$^-$; Figure S12: (a) thermodynamic speciation of **2**$^{2-}$. (The anionic nature of all structure reported is implicit, thus omitted for clarity). (b) Theoretical IR spectrum in the νCO region (in CH_2Cl_2) of **2a**$^{2-}$; Figure S13: (a) thermodynamic speciation of **2**$^{3-}$. (The anionic nature of all structure reported is implicit, thus omitted for clarity). (b) Theoretical IR spectrum in the νCO

region (in CH_2Cl_2) of $2a^{3-}$. (c) Spin density plot of 2^{3-}; Figure S14: thermodynamic speciation of $1H^-$. (The anionic nature of all structure reported is implicit, thus omitted for clarity); Figure S15: spin density plot of $1H^{2-}$ (a) and $1H_2^-$ (b); Figure S16: thermodynamic speciation of $1H_2^-$. (The anionic nature of all structure reported is implicit, thus omitted for clarity).

Appendix A

*Synthesis of [Fe₂(CO)₄(κ²-pma)(μ-bdt)] (Complex **1**)*

A solution of $[Fe_2(CO)_6(\mu\text{-bdt})]$ (500 mg, 1.19 mmol) and two equiv. of trans-N-(2-pyridylmethylene) aniline (434 mg, 2.38 mmol) in toluene (20 mL) was prepared. The resulting red solution was irradiated for 6 hrs at 365 nm (150 W) with a photochemical reactor (mercury lamp). Then, the solvent was removed under reduced pressure. The greenish black residue was purified by chromatography on alumina column. The complex **1** was eluted with a mixture of toluene/dichloromethane (8:2). After evaporation of the solvents, **1** was isolated as a dark green powder (273 mg, 0.5 mmol, 42.0% yield). Crystallization from slow evaporation at $-30\,^\circ$C (hexane/dichloromethane 1:1) afforded dark green crystals.

IR (CH_2Cl_2, cm^{-1}): ν(CO) 2022 (vs), 1956(s), 1924(s).
^{1}H NMR (CD_2Cl_2, δ, ppm) (ill-resolved spectrum): δ 8.48 (br, 1H), 8.43 (br, 1H), 7.90 (br, 1H), 7.68 (br, 1H), 7.50 (br, 2H), 7.41, 7.37 (br, 3H), 7.13 (br, 2H), 6.92 (br, 1H), 6.54 (br, 2H): pma + bdt
^{13}C-{^{1}H} NMR (CD_2Cl_2, δ, ppm): δ 216.3 (CO), 211.6(3xCO), [157.2, 156.3, 152.5, 151.8, 151.2, 132.5, 128.4, 127.7, 127.6, 126.5, 125.1, 124.1, 121.6] (pma + bdt)
Elemental Analysis for $C_{22}H_{14}Fe_2N_2O_4S_2$: 48.33% C, 2.56% H, 5.13% N
Found 47.44% C, 2.50% H, 5.05% N

*Synthesis of [Fe₂(CO)₄(κ²-pma)(μ-pdt)] (Complex **2**)*

To a Schlenk (Roth, Germany) flask, the complex $[Fe_2(CO)_6(\mu\text{-pdt})]$ (500 mg, 1.30 mmol) and 2 equiv. of trans-N-(2-Pyridylmethylene) aniline (474 mg, 2.60 mmol) were added. The Schlenk flask was then purged with argon and 20 mL of degassed anhydrous toluene was added. This red solution was irradiated for 6 hrs at 365 nm (150 W) with a photochemical reactor (mercury lamp). The solvent was then evaporated to dryness. The resulting greenish black residue was purified by column chromatography on alumina. Complex **2** was eluted with a mixture of toluene/dichloromethane (8:2). Then, it was isolated as a dark green powder (366 mg, 0.72 mmol, 55.0% yield) after evaporation of the solvents to dryness. Crystallization from slow evaporation at $-30\,^\circ$C (hexane/dichloromethane 1:1) gave small dark green crystals.

IR (CH_2Cl_2, cm^{-1}): ν(CO) 2014 (vs), 1946(s), 1904(s).

^{1}H NMR (CD$_2$Cl$_2$, δ, ppm): δ [8.77 (d, *J* = 5 Hz, 1H), 8.56 (s, 1H), 7.84 (d, *J* = 10 Hz, 1H), 7.65 (m, 1H), 7.41 (m, 4H), 7.35 (m, 1H), 7.17 (m, 1H)] (pma); [2.20 (m, 1H), 2.02 (m, 1H), 1.91 (m, 1H), 1.74 (m, 1H), 1.50 (m, obscured, 1H) 1.12 ((m, 1H)] (pdt).

^{13}C-{^{1}H} NMR (CD$_2$Cl$_2$, δ, ppm): δ 215. 8 (CO), 212.7 (3xCO), [157.6, 156.6, 152.9, 150.8, 132.5, 128.8, 128.6, 127.6, 124.7, 121.1] (pma); [30.4, 24.7, 24.3] (pdt)

Elemental Analysis calculated for C$_{19}$H$_{16}$Fe$_2$N$_2$O$_4$S$_2$: 44.52% C, 3.12% H, 5.47% N

Found 45.46% C, 3.14% H, 5.26% N

References

1. Peters, J.W.; Lanzilotta, W.N.; Lemon, B.J.; Seefeldt, L.C. X-ray crystal structure of the Fe-only hydrogenase (Cpl) from Clostridium pasteurianum to 1.8 Angstrom resolution. *Science* **1998**, *282*, 1853–1858. [CrossRef]

2. Nicolet, Y.; Piras, C.; Legrand, P.; Hatchikian, C.E.; Fontecilla-Camps, J.C. Desulfovibrio desulfuricans iron hydrogenase: The structure shows unusual coordination to an active site Fe binuclear center. *Structure* **1999**, *7*, 13–23. [CrossRef] [PubMed]

3. Berggren, G.; Adamska, A.; Lambertz, C.; Simmons, T.R.; Esselborn, J.; Atta, M.; Gambarelli, S.; Mouesca, J.M.; Reijerse, E.; Lubitz, W.; et al. Biomimetic assembly and activation of [FeFe]-hydrogenases. *Nature* **2013**, *4*, 66–70. [CrossRef] [PubMed]

4. Lubitz, W.; Ogata, H.; Rüdiger, O.; Reijerse, E. Hydrogenases. *Chem. Rev.* **2014**, *114*, 4081–4148. [CrossRef] [PubMed]

5. Wittkamp, F.; Senger, M.; Stripp, S.T.; Apfel, U.-P. [FeFe]-Hydrogenases: Recent developments and future perspectives. *Chem. Commun.* **2018**, *54*, 5934–5942. [CrossRef]

6. Laun, K.; Baranova, I.; Duan, J.; Kertess, L.; Wittkamp, F.; Apfel, U.-P.; Happe, T.; Senger, M.; Stripp, S.T. Site-selective protonation of the one-electron reduced cofactor in [FeFe]-hydrogenase. *Dalton Trans.* **2021**, *50*, 3641–3650. [CrossRef] [PubMed]

7. Birrell, J.A.; Rodríguez-Maciá, P.; Reijerse, E.J.; Martini, M.A.; Lubitz, W. The catalytic cycle of [FeFe] hydrogenase: A tale of two sites. *Coord. Chem. Rev.* **2021**, *449*, 214191. [CrossRef]

8. Caserta, G.; Zuccarello, L.; Barbosa, C.; Silveira, C.M.; Moe, E.; Katz, S.; Hildebrandt, P.; Zebger, I.; Todorovic, S. Unusual structures and unknown roles of FeS clusters in metalloenzymes seen from a resonance Raman spectroscopic perspective. *Coord. Chem. Rev.* **2022**, *452*, 214287. [CrossRef]

9. Hogarth, G. An unexpected leading role for [Fe$_2$(CO)$_6$(μ-pdt)] in our understanding of [FeFe]-H$_2$ases and the search for clean hydrogen production. *Coord. Chem. Rev.* **2023**, *490*, 215174. [CrossRef]

10. Tard, C.; Liu, X.; Ibrahim, S.K.; Bruschi, M.; De Gioia, L.; Davies, S.C.; Yang, X.; Wang, L.S.; Sawers, G.; Pickett, C.J. Synthesis of the H-cluster framework of iron-only hydrogenase. *Nature* **2005**, *433*, 610–613. [CrossRef]

11. Jørgensen, C.K. Differences between the four halide ligands, and discussion remarks on trigonal-bipyramidal complexes, on oxidation states, and on diagonal elements of one electron energy. *Coord. Chem. Rev.* **1966**, *1*, 164–178. [CrossRef]

12. Elleouet, C.; Pétillon, F.Y.; Schollhammer, P. Role of a redox-active ligand close to a dinuclear activating framework. In *Modes of Cooperative Effects in Dinuclear Complexes*; Kalck, P., Ed.; Topics in Organometallic Chemistry; Springer: Cham, Switzerland, 2023; Volume 70, pp. 99–156. [CrossRef]

13. Becker, R.; Amirjalayer, S.; Li, P.; Woutersen, S.; Reek, J.N.H. An iron-iron hydrogenase mimic with appended electron reservoir for efficient proton reduction in aqueous media. *Sci. Adv.* **2016**, *2*, e1501014. [CrossRef] [PubMed]

14. Camara, J.M.; Rauchfuss, T.B. Combining acid–base, redox and substrate binding functionalities to give a complete model for the [FeFe]-hydrogenase. *Nat. Chem.* **2011**, *4*, 26–30. [CrossRef] [PubMed]

15. Roy, S.; Laureanti, J.A.; Groy, T.L.; Jones, A.K. Synthesis and electrocatalytic activity of [FeFe]-hydrogenase model complexes with non-innocent chelating nitrogen-donor ligands. *Eur. J. Inorg. Chem.* **2017**, *2017*, 2942–2950. [CrossRef]

16. Roy, S.; Groy, T.L.; Jones, A.K. Biomimetic model for [FeFe]-hydrogenase: Asymmetrically disubstituted diiron complex with a redox-active 2,2′-bipyridyl ligand. *Dalton Trans.* **2013**, *42*, 3843–3853. [CrossRef] [PubMed]

17. Ghosh, S.; Rahaman, A.; Holt, K.B.; Nordlander, E.; Richmond, M.G.; Kabir, S.E.; Hogarth, G. Hydrogenase biomimetics with redox-active ligands: Electrocatalytic proton reduction by [Fe$_2$(CO)$_4$(κ^2-diamine)(μ-edt)] (diamine = 2,2′-bipy, 1,10-phen). *Polyhedron* **2016**, *116*, 127–135. [CrossRef]

18. Arrigoni, F.; Elleouet, C.; Mele, A.; Pétillon, F.Y.; De Gioia, L.; Schollhammer, P.; Zampella, G. Insights into the two-electron reductive process of [FeFe]H$_2$ase biomimetics: Cyclic voltammetry and DFT investigation on chelate control of redox properties of [Fe$_2$(CO)$_4$(κ^2-chelate)(μ-dithiolate)]. *Chem. Eur. J.* **2020**, *26*, 17536–17545. [CrossRef]

19. Marx, M.; Mele, A.; Spannenberg, A.; Steinlechner, C.; Junge, H.; Schollhammer, P.; Beller, M. Addressing the reproducibility of photocatalytic carbon dioxide reduction. *ChemCatChem* **2020**, *12*, 1603–1608. [CrossRef]

20. Orain, P.-Y.; Capon, J.-F.; Kervarec, N.; Gloaguen, F.; Pétillon, F.; Pichon, R.; Schollhammer, P.; Talarmin, J. Use of 1,10-phenanthroline in diiron dithiolate derivatives related to the [Fe–Fe] hydrogenase active site. *Dalton Trans.* **2007**, 3754–3756. [CrossRef]

21. Ezzaher, S.; Orain, P.-Y.; Capon, J.-F.; Gloaguen, F.; Pétillon, F.Y.; Roisnel, T.; Schollhammer, P.; Talarmin, J. First insights into the protonation of dissymetrically disubstituted di-iron azadithiolate models of the [FeFe]H$_2$ases active site. *Chem. Commun.* **2008**, 2547–2549. [CrossRef]

22. Seidel, R.A.; Hall, M.B.; Swenson, M.T.; Nichol, G.S.; Lichtenberger, D.L.; Evans, D.H.; Glass, R.S. Synthesis and characterization of [FeFe]-hydrogenase mimics appended with a 2-phenylazopyridine ligand. *J. Sulfur Chem.* **2013**, *34*, 566–579. [CrossRef]

23. Si, Y.; Charreteur, K.; Capon, J.-F.; Gloaguen, F.; Pétillon, F.Y.; Schollhammer, P.; Talarmin, J. Non-innocent bma ligand in a dissymetrically disubstituted diiron dithiolate related to the active site of the [FeFe] hydrogenases. *J. Inorg. Biochem.* **2010**, *104*, 1038–1042. [CrossRef] [PubMed]

24. Greco, C.; De Gioia, L. A theoretical study on the enhancement of functionally relevant electron transfers in biomimetic models of [FeFe]-hydrogenases. *Inorg. Chem.* **2011**, *50*, 6987–6995. [CrossRef] [PubMed]

25. Ghosh, S.; Hollingworth, N.; Warren, M.; Hvorat, D.A.; Richmond, M.G.; Hogarth, G. Hydrogenase biomimics containing redox-active ligands: $Fe_2(CO)_4(\mu\text{-edt})(\kappa^2\text{-bpcd})$ with electron-acceptor 4,5-bis(diphenylphosphino)-4-cyclopenten-1,3-dione (bpcd) as a potential $[Fe_4\text{–}S_4]_H$ surrogate. *Dalton Trans.* **2019**, *48*, 6051–6060. [CrossRef]

26. Morvan, D.; Capon, J.-F.; Gloaguen, F.; Le Goff, A.; Marchivie, M.; Michaud, F.; Schollhammer, F.; Talarmin, J.; Yaouanc, J.-J.; Pichon, R.; et al. N-heterocyclic carbene ligands in nonsymmetric diiron models of hydrogenase active sites. *Organometallics* **2007**, *26*, 2042–2052. [CrossRef]

27. Chouffai, D.; Zampella, G.; Capon, J.-F.; De Gioia, L.; Le Goff, A.; Pétillon, F.Y.; Schollhammer, P.; Talarmin, J. Electrochemical and theoretical studies of the impact of the chelating ligand on the reactivity of $[Fe_2(CO)_4(\kappa^2\text{-LL})(\mu\text{-pdt})]^+$ complexes with different substrates (LL = $I_{Me}\text{-CH}_2\text{-}I_{Me}$, dppe; I_{Me} = 1-methylimidazol-2-ylidene). *Organometallics* **2012**, *31*, 1082–1091. [CrossRef]

28. Arrigoni, F.; De Gioia, L.; Elleouet, C.; Pétillon, F.Y.; Schollhammer, P.; Talarmin, J.; Zampella, G. Normal vs. inverted ordering of reduction potentials in [FeFe]-hydrogenases biomimetics: Effect of the dithiolate bulk. *Chem. Eur. J.* **2023**, *29*, e202300569. [CrossRef]

29. Spall, S.J.P.; Keane, T.; Tory, J.; Cocker, D.C.; Adams, H.; Fowler, H.; Meijer, A.J.H.M.; Hartl, F.; Weinstein, J.A. Manganese tricarbonyl complexes with asymmetric 2-iminopyridine ligands: Toward decoupling steric and electronic factors in electrocatalytic CO_2 reduction. *Inorg. Chem.* **2016**, *55*, 12568–12582. [CrossRef]

30. Lu, C.C.; Weyhermüller, T.; Bil, E.; Wieghardt, K. Accessing the different redox states of α-iminopyridines within cobalt complexes. *Inorg. Chem.* **2009**, *48*, 6055–6064. [CrossRef]

31. Shejwalkar, P.; Rath, N.P.; Bauer, E.B. New iron(II) a-iminopyridine complexes and their catalytic activity in the oxidation of activated methylene groups and secondary alcohols to ketones. *Dalton Trans.* **2011**, *40*, 7617–7631. [CrossRef]

32. Sieh, D.; Lacy, D.C.; Peters, J.C.; Kubiak, C.P. Reduction of CO_2 by pyridine monoimine molybdenum carbonyl complexes: Cooperative metal–ligand binding of CO_2. *Chem. Eur. J.* **2015**, *21*, 8497–8503. [CrossRef] [PubMed]

33. Zhao, Y.; Truhlar, D.G. The M06 suite of density functionals for main group thermochemistry, thermochemical kinetics, noncovalent interactions, excited states, and transition elements: Two new functionals and systematic testing of four M06-class functionals and 12 other functionals. *Theor. Chem. Acc.* **2008**, *120*, 215–241. [CrossRef]

34. Orain, P.-Y.; Capon, J.-F.; Gloaguen, F.; Pétillon, F.Y.; Schollhammer, P.; Talarmin, J.; Zampella, G.; De Gioia, L.; Roisnel, T. Investigation on the protonation of a trisubstituted $[Fe_2(CO)_3(PPh_3)(\kappa^2\text{-phen})(\mu\text{-pdt})]$ complex: Rotated versus unrotated Intermediate pathways. *Inorg. Chem.* **2010**, *49*, 5003–5008. [CrossRef] [PubMed]

35. Capon, J.-F.; Gloaguen, F.; Schollhammer, P.; Talarmin, J. Electrochemical proton reduction by thiolate-bridged hexacarbonyldiiron clusters. *J. Electroanal. Chem.* **2004**, *566*, 241–247. [CrossRef]

36. Capon, J.-F.; Gloaguen, F.; Schollhammer, P.; Talarmin, J. Activation of proton by the two-electron reduction of a di-iron organometallic complex. *J. Electroanal. Chem.* **2006**, *595*, 47–52. [CrossRef]

37. Felton, G.A.N.; Vannucci, A.K.; Chen, J.; Tori Lockett, L.; Okumura, N.; Petro, B.J.; Zakai, U.I.; Evans, D.H.; Glass, R.S.; Lichtenberger, D.L. Hydrogen generation from weak acids: Electrochemical and computational studies of a diiron hydrogenase mimic. *J. Am. Chem. Soc.* **2007**, *129*, 12521–12530. [CrossRef] [PubMed]

38. Windhager, J.; Rudolph, M.; Braütigam, S.; Görls, H.; Weigand, W. Reactions of 1,2,4-trithiolane, 1,2,5-trithiepane, 1,2,5-trithiocane and 1,2,6-trithionane with nonacarbonyldiiron: Structural determination and electrochemical investigation. *Eur. J. Inorg. Chem.* **2007**, *2007*, 2748–2760. [CrossRef]

39. Almazahreh, L.R.; Arrigoni, F.; Abul-Futouh, H.; El-Khateeb, M.; Görls, H.; Elleouet, C.; Schollhammer, P.; Bertini, L.; De Gioia, L.; Rudolph, M.; et al. Proton shuttle mediated by $(SCH_2)_2P{=}O$ moiety in [FeFe]-hydrogenase mimics: Electrochemical and DFT studies. *ACS Catal.* **2021**, *11*, 7080–7098. [CrossRef]

40. Arrigoni, F.; Rizza, F.; Vertemara, J.; Breglia, R.; Greco, C.; Bertini, L.; Zampella, G.; De Gioia, L. Rational Design of $Fe_2(\mu\text{-PR}_2)_2(L)_6$ coordination compounds featuring tailored potential inversion. *ChemPhysChem* **2020**, *21*, 2279–2292. [CrossRef]

41. Wright, R.J.; Zhang, W.; Yang, X.; Fasuloa, M.; Tilley, T.D. Isolation, observation, and computational modeling of proposed intermediates in catalytic proton reductions with the hydrogenase mimic $Fe_2(CO)_6S_2C_6H_4$. *Dalton Trans.* **2012**, *41*, 73–82. [CrossRef]

42. Mirmohades, M.; Pullen, S.; Stein, M.; Maji, S.; Ott, S.; Hammarström, L.; Lomoth, R. Direct observation of key catalytic intermediates in a photoinduced proton reduction cycle with a diiron carbonyl complex. *J. Am. Chem. Soc.* **2014**, *136*, 17366–17369. [CrossRef] [PubMed]

43. Etinski, M.; Stanković, I.M.; Rakesh, C.; Puthenkalathil, R.C.; Ensing, B. A DFT study of structure and electrochemical properties of diiron-hydrogenase models with benzenedithiolato and benzenediselenato ligands. *New J. Chem.* **2020**, *44*, 932–941. [CrossRef]

44. Gao, S.; Liang, Q.; Duan, Q.; Jiang, D.; Zhao, J. Electrochemical proton reductions in varying acidic media by a simple synthetic hydrogenase mimic. *Int. J. Hydrogen Energy* **2018**, *43*, 7245–7256. [CrossRef]

45. Winter, A.; Zsolnai, L.; Huttner, G. Dinuclear and trinuclear carbonyliron complexes containing 1,2- and 1,3-dithiolato bridging ligands. *Z. Naturforsch* **1982**, *37b*, 1430–1436. [CrossRef]

46. Lyon, E.J.; Georgakaki, I.P.; Reibenspies, J.H.; Darensbourg, M.Y. Coordination sphere flexibility of active-site models for Fe-only hydrogenase: Studies in intra- and intermolecular diatomic ligand exchange. *J. Am. Chem. Soc.* **2001**, *123*, 3268–3278. [CrossRef]

47. Cabeza, J.A.; Martinez-Garcia, M.A.; Riera, V.; Ardura, D.; Garcia-Granda, S. Binuclear iron(I), ruthenium(I), and osmium(I) hexacarbonyl complexes containing a bridging benzene-1,2-dithiolate ligand. Synthesis, X-ray structures, protonation reactions, and EHMO calculations. *Organometallics* **1998**, *17*, 1471–1477. [CrossRef]

48. Arrigoni, F.; Mohamed Bouh, S.; Elleouet, C.; Pétillon, F.Y.; Schollhammer, P.; De Gioia, L.; Zampella, G. Electrochemical and theoretical investigations of the oxidatively induced reactivity of the complex [Fe$_2$(CO)$_4$(κ^2-dmpe)(μ-adtBn)] related to the active site of [FeFe] hydrogenases. *Chem. Eur. J.* **2018**, *24*, 15036–15051. [CrossRef] [PubMed]

49. Farrugia, L.J. WinGX suite for small molecule single-crystal crystallography. *J. Appl. Cryst.* **1999**, *32*, 837–838. [CrossRef]

50. Ahlrichs, R.; Bär, M.; Häser, M.; Horn, H.; Kölmel, C. Electronic structure calculations on workstation computers: The program system Turbomole. *Chem. Phys. Lett.* **1989**, *162*, 165–169. [CrossRef]

51. Becke, A.D. Density-functional exchange-energy approximation with correct asymptotic behavior. *Phys. Rev. A At. Mol. Opt. Phys.* **1988**, *38*, 3098–3100. [CrossRef]

52. Perdew, J.P. Density-functional approximation for the correlation energy of the inhomogeneous electron gas. *Phys. Rev. B Condens. Matter Mater. Phys.* **1986**, *33*, 8822–8824. [CrossRef] [PubMed]

53. Schäfer, A.; Huber, C.; Ahlrichs, R. Fully optimized contracted Gaussian basis sets of triple zeta valence quality for atoms Li to Kr. *J. Chem. Phys.* **1994**, *100*, 5829–5835. [CrossRef]

54. Chatelain, L.; Breton, J.-B.; Arrigoni, F.; Shollhammer, P.; Zampella, G. Geometrical influence on the non-biomimetic heterolytic splitting of H$_2$ by bio-inspired [FeFe]-hydrogenase complexes: A rare example of inverted frustrated Lewis pair based reactivity. *Chem. Sci.* **2022**, *13*, 4863–4873. [CrossRef] [PubMed]

55. Arrigoni, F.; Bertini, L.; Breglia, R.; Greco, C.; De Gioia, L.; Zampella, G. Catalytic H$_2$ evolution/oxidation in [FeFe]-hydrogenase biomimetics: Account from DFT on the interplay of related issues and proposed solutions. *New J. Chem.* **2020**, *44*, 17596–17615. [CrossRef]

56. Chambers, J.M.; Rauchfuss, T.B.; Arrigoni, F.; Zampella, G. Effect of pyramidalization of the M$_2$(SR)$_2$ center: The case of (C$_5$H$_5$)$_2$Ni$_2$(SR)$_2$. *Organometallics* **2016**, *35*, 836–846. [CrossRef]

57. Arrigoni, F.; Mohamed Bouh, S.; De Gioia, L.; Elleouet, C.; Pétillon, F.Y.; Schollhammer, P.; Zampella, G. Influence of the dithiolate bridge on the oxidative processes of diiron models related to the active site of [FeFe] hydrogenases. *Chem.-Eur. J.* **2017**, *23*, 4364–4372. [CrossRef]

58. Eichkorn, K.; Weigend, F.; Treutler, O.; Ahlrichs, R. Auxiliary basis sets for main row atoms and transition metals and their use to approximate coulomb potentials. *Theor. Chem. Acc.* **1997**, *97*, 119–124. [CrossRef]

59. Grimme, S.; Antony, J.; Ehrlich, S.; Krieg, H. A consistent and accurate ab initio parametrization of density functional dispersion correction (DFT-D) for the 94 elements H-Pu. *J. Chem. Phys.* **2010**, *132*, 154104–154122. [CrossRef]

60. Grimme, S.; Ehrlich, S.; Goerigk, L. Effect of the damping function in dispersion corrected density functional theory. *J. Comput. Chem.* **2011**, *32*, 1456–1465. [CrossRef]

61. Klamt, A. Conductor-like screening model for real solvents: A new approach to the quantitative calculation of solvation phenomena. *J. Phys. Chem.* **1995**, *99*, 2224–2235. [CrossRef]

62. Klamt, A. Calculation of UV/Vis spectra in solution. *J. Phys. Chem.* **1996**, *100*, 3349–3353. [CrossRef]